
This is an electronic reprint of the original article.

This reprint may differ from the original in pagination and typographic detail.

Kontula, J.; Äkäslompolo, S.; Ikäheimo, A.; Lazerson, S.; Kurki-Suonio, T.; Hartmann, D.; Rust, N.; McNeely, P.; Kazakov, Ye O.; Ongena, J.; W7-X Team

Predictive simulations of NBI ion power load to the ICRH antenna in Wendelstein 7-X

Published in:

Plasma Physics and Controlled Fusion

DOI:

[10.1088/1361-6587/acd07e](https://doi.org/10.1088/1361-6587/acd07e)

Published: 01/07/2023

Document Version

Publisher's PDF, also known as Version of record

Published under the following license:

CC BY

Please cite the original version:

Kontula, J., Äkäslompolo, S., Ikäheimo, A., Lazerson, S., Kurki-Suonio, T., Hartmann, D., Rust, N., McNeely, P., Kazakov, Y. O., Ongena, J., & W7-X Team (2023). Predictive simulations of NBI ion power load to the ICRH antenna in Wendelstein 7-X. *Plasma Physics and Controlled Fusion*, 65(7), 1-11. Article 075008. <https://doi.org/10.1088/1361-6587/acd07e>

PAPER • OPEN ACCESS

Predictive simulations of NBI ion power load to the ICRH antenna in Wendelstein 7-X






To cite this article: J Kontula *et al* 2023 *Plasma Phys. Control. Fusion* **65** 075008

View the [article online](#) for updates and enhancements.

You may also like

- [The geometry of the ICRF-induced wave-SOL interaction. A multi-machine experimental review in view of the ITER operation](#)
L. Colas, G. Urbanczyk, M. Goniche et al.
- [ICRH antenna S-matrix measurements and plasma coupling characterisation at JET](#)
I. Monakhov, P. Jacquet, T. Blackman et al.
- [Design and operations of a load-tolerant external conjugate-T matching system for the A2 ICRH antennas at JET](#)
I. Monakhov, M. Graham, T. Blackman et al.

Predictive simulations of NBI ion power load to the ICRH antenna in Wendelstein 7-X

J Kontula^{1,*} , S Äkäslompolo¹ , A Ikäheimo¹, S Lazerson² , T Kurki-Suonio¹, D Hartmann² , N Rust², P McNeely², Ye O Kazakov³, J Ongena³  and the W7-X team⁴

¹ Aalto University, Department of Applied Physics, Espoo, Finland

² Max-Planck-Institut für Plasmaphysik, Greifswald, Germany

³ Laboratory for Plasma Physics, Ecole Royale Militaire-Koninklijke Militaire School, Brussels, Belgium

E-mail: joona.kontula@aalto.fi

Received 10 February 2023, revised 13 April 2023

Accepted for publication 26 April 2023

Published 26 May 2023



Abstract

In Wendelstein 7-X (W7-X), a new ion cyclotron resonance heating (ICRH) antenna will be commissioned during the operational campaign OP2.1. The antenna will have to sustain power loads not only from thermal plasma and radiation but also fast ions. Predictive simulations of fast-ion power loads to the antenna components are therefore important to establish safe operational limits. In this work, the fast-ion power loads from the W7-X neutral beam injection (NBI) system to the ICRH antenna was simulated using the ASCOT suite of codes. Five reference magnetic configurations and five antenna positions were considered to provide an overview of power load behavior under various operating conditions. The NBI power load was found to have an exponential dependence on the antenna insertion depth. Differences between magnetic configurations were significant, with the antenna limiter power load varying between 380 W and 100 kW depending on the configuration. Qualitative differences in power load patterns between configurations were also observed, with the low mirror and low iota configurations exhibiting higher loads to the sensitive antenna straps. The local fast-ion power flux to the antenna limiter was also considered and found to exceed the 2.0 MW m^{-2} steady-state safety limit only in specific cases. The NBI system might thus pose a safety concern to the ICRH antenna during concurrent NBI-ICRH operation, but additional heat propagation simulations of antenna components are needed to establish more realistic operational time limits.

Keywords: NBI, ICRH, fast ions, Wendelstein 7-X, stellarator, ASCOT

(Some figures may appear in colour only in the online journal)

⁴ See Sunn Pedersen *et al* 2022 (<https://doi.org/10.1088/1741-4326/ac2cf5>) for the W7-X Team.

* Author to whom any correspondence should be addressed.



Original Content from this work may be used under the terms of the [Creative Commons Attribution 4.0 licence](https://creativecommons.org/licenses/by/4.0/). Any further distribution of this work must maintain attribution to the author(s) and the title of the work, journal citation and DOI.

1. Introduction

The Wendelstein 7-X (W7-X) stellarator at the Max Planck Institute for Plasma Physics in Greifswald, Germany [1] represents the cutting edge in stellarator optimization and design. As the largest and most advanced stellarator to date, it represents a crucial step towards a future stellarator fusion reactor.

Efficient operation of plasma heating systems is the key to achieving higher performance plasmas in W7-X. To date, the most established source of plasma heating in W7-X is the electron cyclotron resonance heating (ECRH) system. In addition, a neutral beam injection (NBI) system has been commissioned, providing a source of ion heating as well [2].

All ion heating systems rely on highly energetic ions depositing their kinetic energy to the bulk plasma particles. This principle implies the existence of a fast-ion minority population in the plasma. These highly energetic fast ions behave differently to the bulk ions, residing in different collisionality regimes. Stellarators in particular require careful magnetic field optimization to provide adequate confinement of fast ions in reactor-relevant conditions [3].

The precarious confinement of fast ions means that, even at small quantities, they can result in significant power loads to the device wall. These loads can be highly concentrated to specific ‘hot spots’ due to the localized nature of fast-ion loss channels, such as magnetic islands and ripple wells. Accurate local prediction of fast-ion wall loads has thus been a subject of many fast-ion simulations in W7-X [3, 4]. Such simulations have already provided important predictions and resulted in armoring of new components before installation [5].

In the next W7-X campaign, a new ion heating system—ion cyclotron resonance heating (ICRH)—will be commissioned [6]. This not only provides a new source of fast ions in the device, but also a new, delicate component that might be subject to fast-ion power loads. The aim of this study is to provide an initial estimate of the NBI-driven power load to the new ICRH antenna.

The structure of the paper is as follows. In section 2, the ICRH (section 2.1) and NBI (section 2.2) heating systems are described. Section 3 outlines the numerical methods and input data used for simulating the NBI power loads. The results are presented in section 4, while section 5 gives a summary and analysis of the results, together with possible future improvements upon this work.

2. Ion heating systems in W7-X

The two methods of ion heating available in W7-X are the ICRH and NBI systems. The toroidal positioning of the systems is illustrated in figure 1. The technical details of the ICRH and NBI systems are defined in sections 2.1 and 2.2, respectively.

2.1. ICRH heating in W7-X

In ICRH, ions in the plasma are heated by radio frequency (RF) waves in the same frequency range as the ion cyclotron motion. The ICRH system comprises an RF generator, transmission

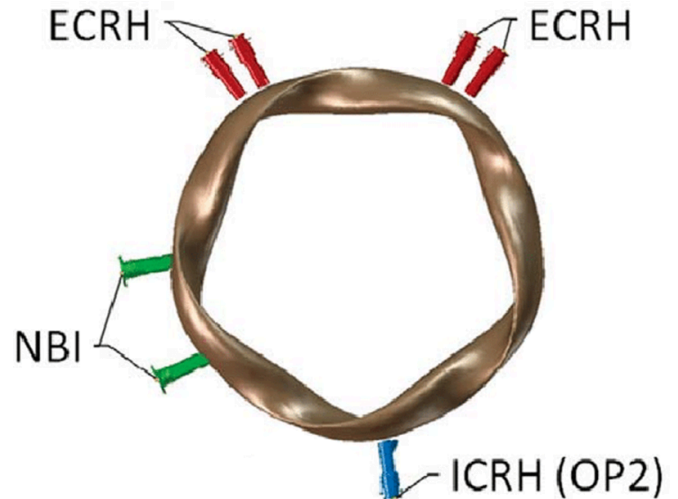


Figure 1. Positions of the plasma heating systems in W7-X [7]. The relevant systems for the calculations here are the NBI system (green) and the ICRH antenna installed in OP2 (blue). Reproduced courtesy of IAEA. Figure from [7]. Copyright (2013) IAEA.

lines to the torus and an in-vessel strip antenna. The antenna has to be placed as close to the plasma as possible for efficient coupling to the plasma while ensuring safe operation. An ICRH system is typically used as a heating system, but it also provides a fast-ion population at energies of around 100 keV. Ions in the 100 keV range in W7-X have approximately the same ratio of gyro radius to machine size as foreseen HELIAS reactors, making them suitable for predicting fast-ion confinement in future reactors [3]. Furthermore, ICRH produces the fast ions on wide banana orbits near the center of the plasma, which are the most critical orbits as far as the optimized fast-ion confinement in stellarators is concerned. Self-consistent simulation of the ICRH heating and the resulting fast-ion population is possible in W7-X using, e.g. the SCENIC package [8, 9].

The ICRH antenna in W7-X will be in use for Operational Phase 2.1 (OP2.1) [10]. It is designed for up to 1.5 MW of RF power at 25.0 MHz to 37.5 MHz frequencies, transferred to the plasma via two antenna straps. The ICRH antenna shape is optimized for the last closed flux surface (LCFS) of the standard magnetic configuration, but the antenna is radially movable for adapting to different magnetic configurations [11]. Of particular interest for fast-ion loads are the graphite limiter tiles (shown in yellow in figure 2) and the antenna straps (shown in green). The water cooled limiter tiles are designed to withstand high power loads of 2 MW m^{-2} from both the thermal bulk plasma and fast ions and protect the sensitive straps from excess heat loads. The straps can withstand 100 kW m^{-2} plasma radiation and 100 kW RF resistive power, while the stainless steel antenna box is designed for loads less than 100 kW m^{-2} [10]. All of these safety limits are estimates for steady-state operation of up to 30 min. By comparison, the maximum NBI pulse length is just 5 s. The actual operational limit to the power loads is ultimately determined by the component temperature, which depends on the exposure

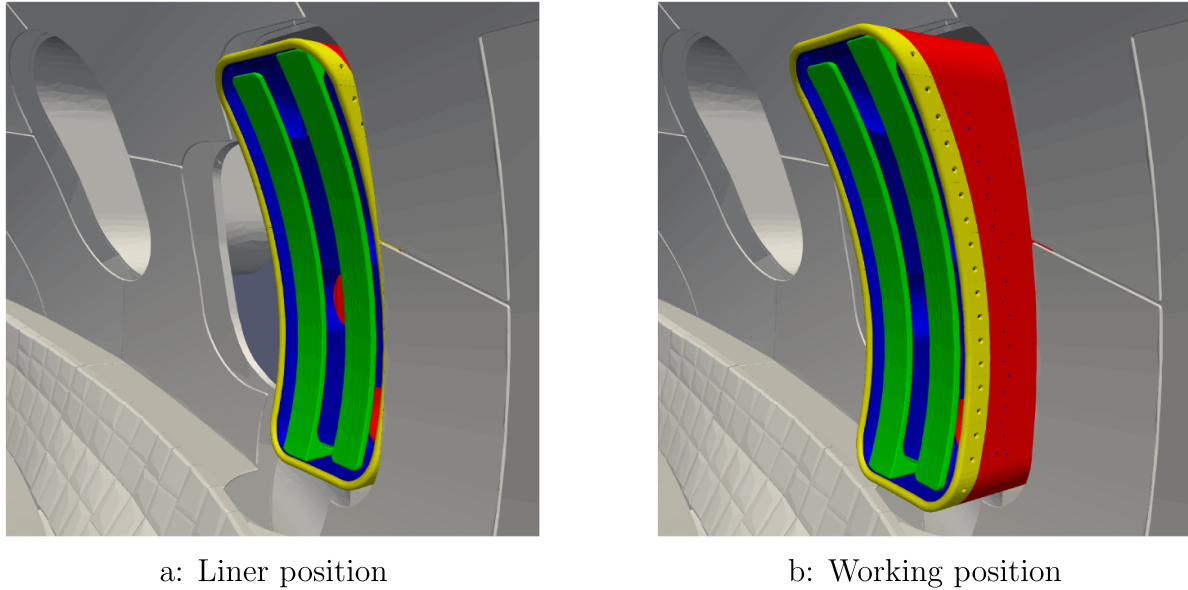


Figure 2. Visualization of the ICRH antenna model used for the simulations in the working position. The model is divided into different components labeled by color: antenna limiter (yellow), antenna straps (green), copper sheath (blue), and antenna box (red). Two positions—the liner position and the working position—are shown.

time as well as the local power flux. With regards to the fast-ion power loads, the limiters are expected to receive the bulk of the power, mainly from fast ions on trapped orbits, but the straps are also likely to be subject to minor loads.

2.2. NBI injection system in W7-X

In parallel to the ICRH system, an NBI system is also installed in W7-X. The principle of the NBI system is that ions are accelerated to high velocities inside an injector and then neutralized. The beam of neutrals then penetrates the plasma until the neutrals are re-ionized, producing a fast-ion population. The planned NBI injection parameters are shown in Table 1 [12]. The W7-X NBI system comprises of two injection boxes, placed symmetrically to avoid unwanted current drive. Each injector has four positive ion neutral injectors (PINIs) at angles of either 17° or 27° from fully perpendicular to the plasma. The NBI system has been operated to date with two PINIs, but will be extended to four PINIs (two in each injection box) in OP2.1 [13]. The maximum capacity is eight PINIs, four in each box. This total number was also chosen for the simulations in order to provide an upper limit to the loads, as well as allow separate assessment of the power load from each of the eight PINIs.

Previous analysis of NBI heat loads in W7-X have been able to qualitatively predict some specific hot spots on the device wall [5, 14]. Quantitative analysis has proved more difficult due to uncertainty in input parameters and some missing key physics models, such as charge exchange (CX) reactions. Nevertheless, predictive modeling of NBI heat loads is needed for any new component—such as the ICRH antenna—to provide a qualitative understanding of the heat load behavior in different magnetic configurations, for example. The missing

Table 1. Planned parameters for W7-X hydrogen neutral beam injection. The species mix denotes the fraction of beam particles born at different divisions of the beam acceleration energy $E_b = 55$ keV.

Acceleration voltage	55 kV
Max. number of PINIs	8
Beam power (all sources)	13.7 MW
Species mix (particle fraction)	55% (E_b); 31% ($E_b/2$); 14% ($E_b/3$)

physical effects would mainly spread out the power loads and thus lower the peak power loads.

3. Numerical approach to NBI wall load modelling

The main simulation tool for the ICRH antenna power load calculations was the ASCOT suite of codes [15]. The core of this suite is ASCOT itself, a Monte Carlo orbit following code used for solving minority species distribution functions in fusion devices. The important, advanced features of ASCOT, crucial for this work, are its capability to follow the beam ions all the way to the plasma-facing components, and that it can track not just the guiding-center orbits but even the full gyro motion. It also allows for accurate assessment of particle and power deposition to the device wall with a full 3D reconstruction of the wall using over 8000 000 triangular wall elements.

The code suite includes also various built-in sources for fast ions [16–18]. The BBNBI code models the NBI system [16] and was used to generate the fast-ion birth profile in this work. In BBNBI, neutral particles are generated in individual beamlets of finite divergence at the grounded grid, with the known fractions of particles with full, one-half and one-third energy. These neutrals are followed in the beam duct that

Table 2. Studied insertion depths of the ICRH antenna.

Name of position	Liner				Working
Insertion depth (mm)	102	189	233	255	277
Normalized insertion depth	0	1/2	3/4	7/8	1

includes the beam scrapers and, once entering the vessel, their ionization probability is evaluated at each time step, using Monte Carlo operator based on local density and temperature values.

To allow accurate calculation of the fast-ion power load distribution on the W7-X ICRH antenna, a two-fold simulation process was adopted. First, ten million markers were created with BBNBI and simulated using the guiding center formalism until they were either thermalized or reached the LCFS. The particles were considered thermalized when their energy was less than twice the local thermal energy. The particles that cross the LCFS were then transformed from guiding-center to full-orbit coordinates [19] and the simulation was continued using the full orbit formalism until they hit either the antenna or the device wall. The particle gyrophase is tracked from the injection to the wall consistently. Some particles that reach the LCFS do not hit the wall or the antenna but instead re-enter the plasma. These particles were stopped after a pre-determined processor time limit of 600 s was exceeded. The re-entering markers account for between 2.8% and 26% of the particles that cross the LCFS.

3.1. Wall and antenna models

The basic wall model of W7-X used in the simulations was constructed from CAD models and includes the entire device first wall, including divertor assemblies and port structures. In addition, a separate model including the full NBI duct geometry was used in the BBNBI simulations to account for beam duct scraping [12, 20, 21].

The ICRH antenna model was imported from a high-detail CAD model in the W7-X component database [22]. The antenna model consists of approximately eight million triangles of varying size with a median triangle area of 7.28 mm². The ICRH antenna structure is comprised of four primary components, illustrated in figure 2. The *antenna straps* (green) are the main functional part of the device, used to transfer power to the plasma. The antenna limiter (yellow) is designed to shield the rest of the antenna, while the antenna box (red) and copper sheath (blue) hold the assembly together.

To assess the effect of antenna insertion depth on the ICRH antenna power loads, several different antenna positions had to be studied. The positions limiting the range of interest with regards to fast ions are the *liner position* and the *working position*, inserted 102 mm and 277 mm from the fully retracted *park position*, respectively. The liner position is designed to sit flush on the first wall of the device, while the working position is designed to be as close as possible to the LCFS of the standard configuration. Between these limits, three additional positions were chosen at increasingly dense intervals to provide

intermediate data points: the different positions are listed in table 2. The combined wall model was constructed by adding the ICRH antenna model to the complete first wall model, with the latter moved the desired distance along the antenna axis of motion.

3.2. Plasma profiles and magnetic backgrounds

Experimental plasma profiles from OP1.2b are either not yet available or have large uncertainties. For this reason, parametric plasma profiles approximating typical ECRH-NBI discharges from OP1.2b were used. The profiles for the electron and ion temperatures and densities were defined as:

$$\begin{aligned}
 T_e(s) &= (1 - \sqrt{s})T_{e,0} \\
 T_i(s) &= \min(T_e(s), 1.5 \text{ keV}) \\
 n_e(s) &= n_{e,0}(3 - s^3)/3 \\
 n_i(s) &= n_e(s).
 \end{aligned} \tag{1}$$

Here s is the normalized toroidal flux and $T_{e,0}$ and $n_{e,0}$ are the desired electron temperature and density at the plasma core. The maximum ion temperature is limited to 1.5 keV to account for experimentally observed ion temperature clamping [23]. The radial electric field, which is paramount for fast-ion confinement in W7-X, was calculated for each plasma profile using the NEOTRANSP transport code [24]. For the central plasma parameters, values of 3.0 keV and $5.0 \times 10^{19} \text{ m}^{-3}$ were chosen to roughly correspond with typical ECRH-NBI discharges from OP1.2b [25]. No impurities were included in the plasma profiles. The full 1D plasma profiles, as well as the NEOTRANSP-calculated derivative of the flux surface potential, are shown in figure 3.

Five magnetic configurations were selected to cover the most common configurations for NBI operation in OP2.1. The configurations were standard (STD) in the center of the parameter space; high mirror (HM) and low mirror (LM) which vary the mirror ratio of the magnetic field; and high iota (HI) and low iota (LI) which have edge ι values of 5/4 and 5/6, respectively. The magnetic geometry consists of a regular and periodic cylindrical grid. There are 276 grid points in the toroidal direction, covering one of the five toroidal sectors. In the radial and height dimensions there are 139 grid points, ranging from 3.8 m to 6.9 m and -1.6 m to 1.6 m , respectively. In total this results in 5.3 million grid points for each toroidal sector, with a mean volume of 12.5 cm³ per grid cell. The magnetic field and by extent the plasma quantities are interpolated to the marker positions using tricubic spline interpolation.

The magnetic configuration has a profound effect on the position of the ICRH antenna with respect to the LCFS. Figure 4 shows the distance of the antenna components from the LCFS as measured by the extrapolated value of the radial flux coordinate ρ . The LM and LI configurations have the least distance between the plasma and the antenna, while the HM and HI configurations are the furthest apart from the LCFS. The standard configuration sits in the middle of these two extremes.

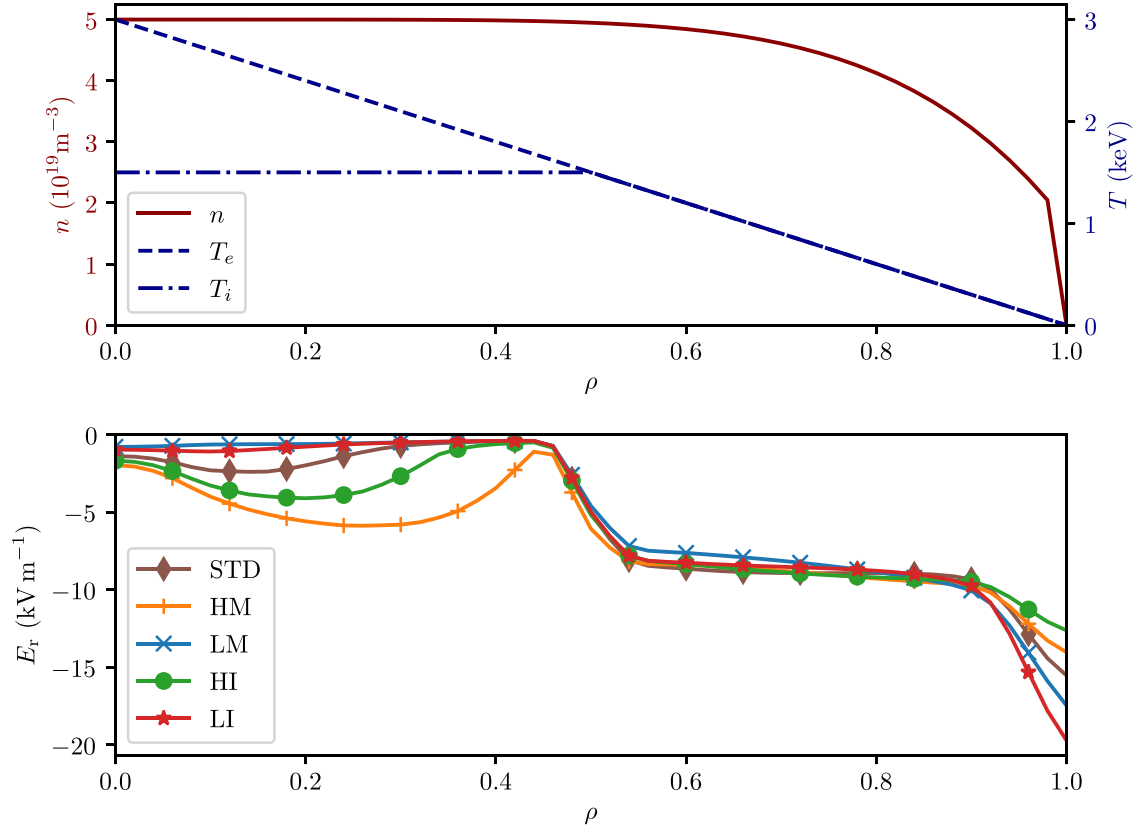


Figure 3. Radial plasma profiles for the ASCOT simulations. The top figure shows the electron and ion density (red) and the electron temperature (solid blue) and ion temperature (dashed blue) profiles, which are defined parametrically by equation (1) and are the same for all magnetic configurations. The radial electric field, shown in the bottom figure, is dependent on the magnetic configuration and calculated separately for each configuration from the temperature and density profiles.

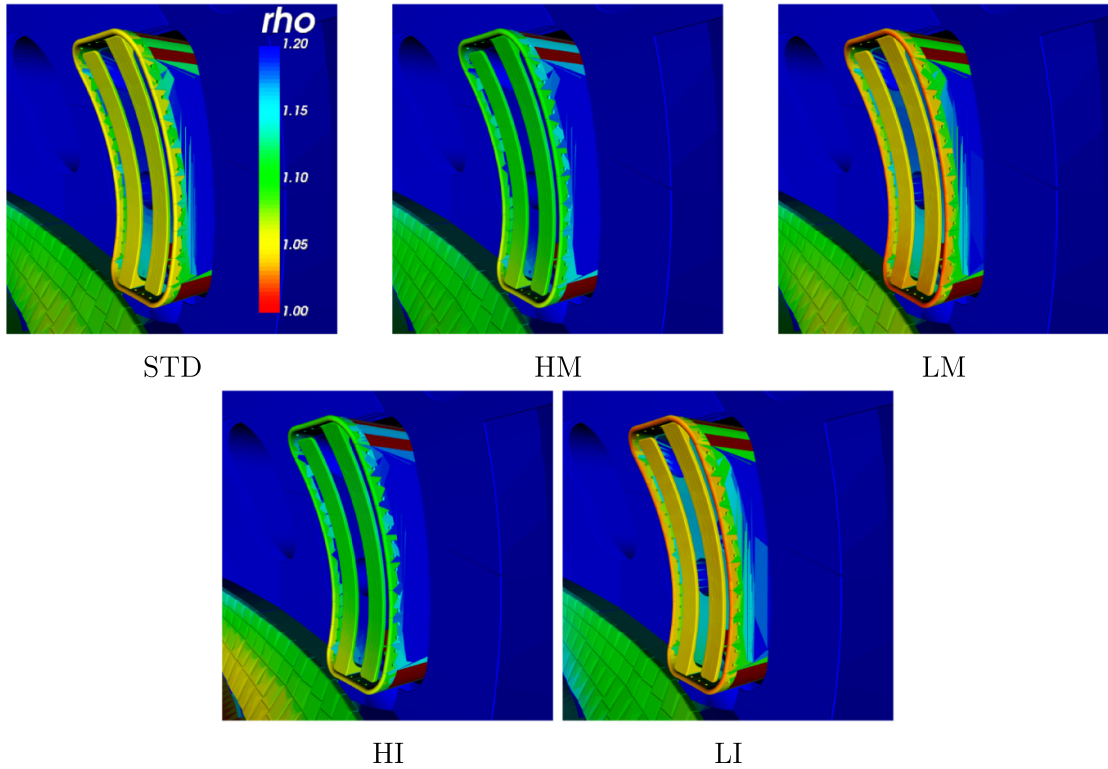


Figure 4. Radial coordinate ρ evaluated at the wall coordinates for the different magnetic configurations. Hot colors are closer to the LCFS and the color axis is the same in all configurations.

4. Results

4.1. Beam slowing-down simulations

The ensemble of 10 M NBI markers were generated with the BBNBI code. The profile was calculated separately for each of the configurations since the shape of the plasma also changes the beam ion birth profile. The radial profiles of the generated NBI ions are shown in figure 5. The highest number of markers are generated in the core plasma ($\rho \leq 0.5$ where the density is highest). This means that the beam ion density is significantly higher in the plasma core, since the volume of the core plasma is much smaller than the edge plasma: only 25% of the total plasma volume is inside the $\rho = 0.5$ flux surface. The ionization profiles have differences due to the shape of the equilibria. As the two extreme cases, in the LI configuration the ions are born further away radially due to the plasma extending farther in major radius, whereas in the HI configuration the ions are born at lower major radii due to the opposite reason. Due to the low density, shinethrough fractions were high, between 25.5% and 27.7% as seen from the ratio of ionized power to the total injected power in table 3. This number includes both beam duct scraping and actual shinethrough, i.e. particles that pass through the plasma as neutrals.

The slowing-down simulation for the beam ions showed considerable differences in beam confinement between different magnetic configurations, as shown in table 3. The HM configuration has the lowest particle loss fraction at 0.75 MW due to the shape of the magnetic field: the plasma equilibrium is smaller in this configuration, and additionally less fast ions are born on trapped orbits in this configuration than in other configurations. The LI configuration has the highest amount of losses at 1.71 MW due to the outward-shifted shape of the plasma. These results are consistent with behavior of fast-ion confinement in earlier simulations [4].

4.2. Simulating the ICRH antenna power load

The fast-ion wall load to the ICRH antenna was simulated using the full-orbit formalism. Significant differences in total antenna loads were found between configurations: the total antenna power load at working position varies from just 0.38 kW in the HI configuration to 99.31 kW in the LM configuration (see table 3). To provide a visual overview of the NBI lost fast-ion power loads on the ICRH antenna, the loads in each of the magnetic configurations are shown in figure 6. As expected from the antenna design, the highest loads in most of the configurations are seen at the limiter tiles. Less intense power loads are also seen at the antenna straps and antenna box. It should be noted that the color axis is logarithmic, so the limiter power loads are around two orders of magnitude higher than the power loads to other components. The copper sheath is only subject to loads at the very upper left-hand corner of the antenna, inside and next to the limiter tiles. In all of the configurations, the other side of the antenna (not shown in figure 6) received significantly smaller losses.

There are both qualitative and quantitative differences in the antenna power loads between magnetic configurations. In

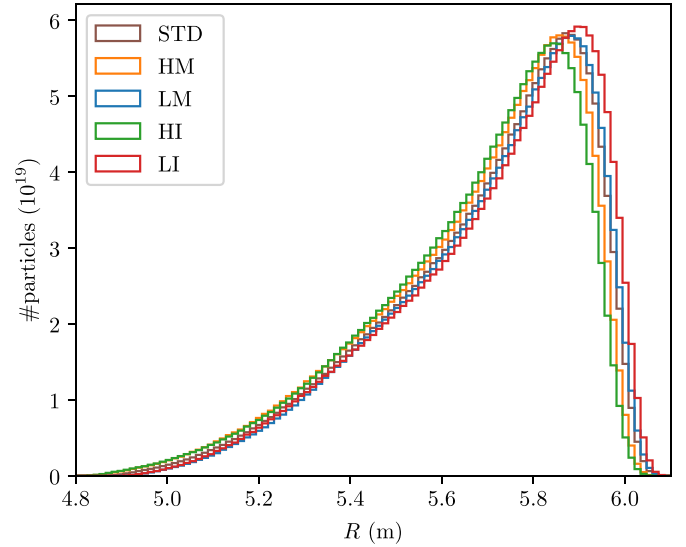


Figure 5. Beam ion birth profiles as a function of the major radius R for the different magnetic configurations. Since the plasma profiles are kept constant the differences between configurations are solely due to the shape of the equilibria.

Table 3. Injected, ionized and lost power and antenna power load at working position in the different magnetic configurations.

	Injected (MW)	Ionized (MW)	Lost (MW)	Antenna (kW)
STD	13.68	10.07	1.52	26.08
HM	13.68	10.16	0.75	14.45
LM	13.68	9.88	1.42	99.31
HI	13.68	9.92	1.24	0.38
LI	13.68	10.19	1.71	91.27

particular, the total wall loads are highest in the LM and LI configurations. This is explained by the relative distance of the antenna to the plasma in these configurations (figure 4). Conversely, the HM and standard configurations have less power load, while the HI configuration sees only negligible losses to the antenna. In the standard configuration a significant number of particles hit the right-hand side of the antenna box. This happens simply due to the magnetic field geometry: in the standard configuration, NBI ion losses to the device steel panels are seen at corresponding parts of the wall in other toroidal sectors. In other configurations these periodic losses are located at other parts of the wall.

To assess the nature of the NBI ions hitting the antenna, the energy-pitch distribution of the particles hitting the antenna was also studied. Figure 7 shows the distribution of NBI ions hitting the antenna in the STD configuration with the antenna in working position. The three injection energy fractions are clearly visible along with slowed-down particles at energies below the three initial energies. There are several weaker peaks in the pitch direction as well, caused by the different orientations of the four PINIs. Particles that hit the antenna have pitch magnitudes between 0.1 and 0.8. This means that passing and toroidally trapped particles are not a major source of antenna loads, and instead the source of the fast-ion losses to the

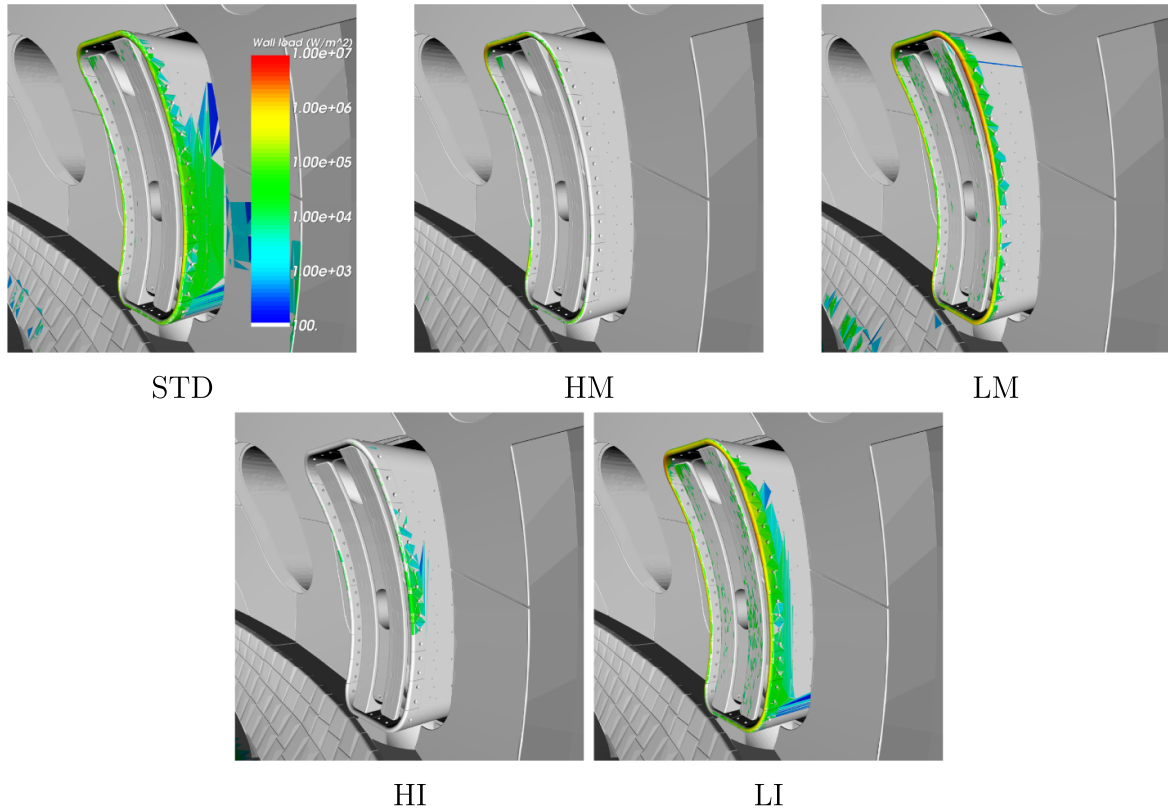


Figure 6. Wall loads to the ICRH antenna for the different magnetic configurations. The color axis is the same in all of the configurations.

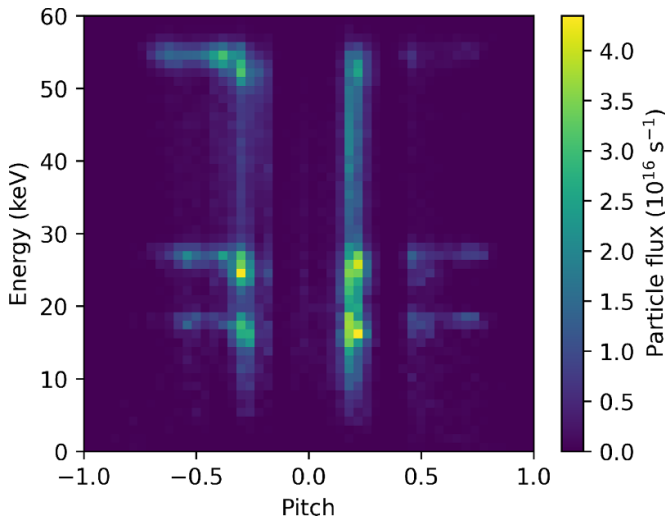


Figure 7. NBI ion flux to the ICRH antenna as a function of the particle pitch and energy in the STD configuration with the antenna in the working position. The nominal injection energies of $E_b = 55$ keV, $E_b/2$ and $E_b/3$ are clearly visible, as well slowed-down particles at low pitch values.

antenna are mostly blocked or helically trapped fast ions [26]. This can be understood from the position of the NBI injectors relative to the ICRH antenna (figure 1). Since the NBI boxes are both located in different toroidal sectors than the ICRH antenna, particles trapped in one toroidal sector have no loss

channels that would reach the antenna. By contrast, particles with pitch magnitude of over 0.80 are well-confined and not lost from the plasma. This leaves a population of helically trapped and passing particles that have a chance to traverse to the ICRH antenna sector and consequently hit the antenna. Most of the antenna losses are prompt losses at almost the full injection energy, with slowed-down particles also hitting the antenna at low magnitudes of particle pitch.

Because the different components of the ICRH antenna have a varying capacity to withstand power loads, it is beneficial to look at the total power load to each of the component types separately. For this analysis, the five different antenna positions mentioned in table 2 were simulated. The total power loads to each component type for all configurations and antenna positions are shown in figure 8. In general, the power load shows an exponential dependence on the antenna insertion depth. The power load is almost zero for half of the distance between the liner and working positions.

The antenna limiter loads are the highest compared to other components, up to 100 kW in total for the LM and LI configurations. The standard and HM configurations have comparable loads of 24 kW and 14 kW, respectively, or around 20% of those in LM and LI. The HI configuration has negligible loads of only up to 380 W at full insertion.

The power loads of the antenna straps follow a similar pattern as the limiter loads. Their magnitude is much lower, however, reaching only up to 0.7 kW total in the LM and LI configurations. According to figure 6, the strap loads are mostly

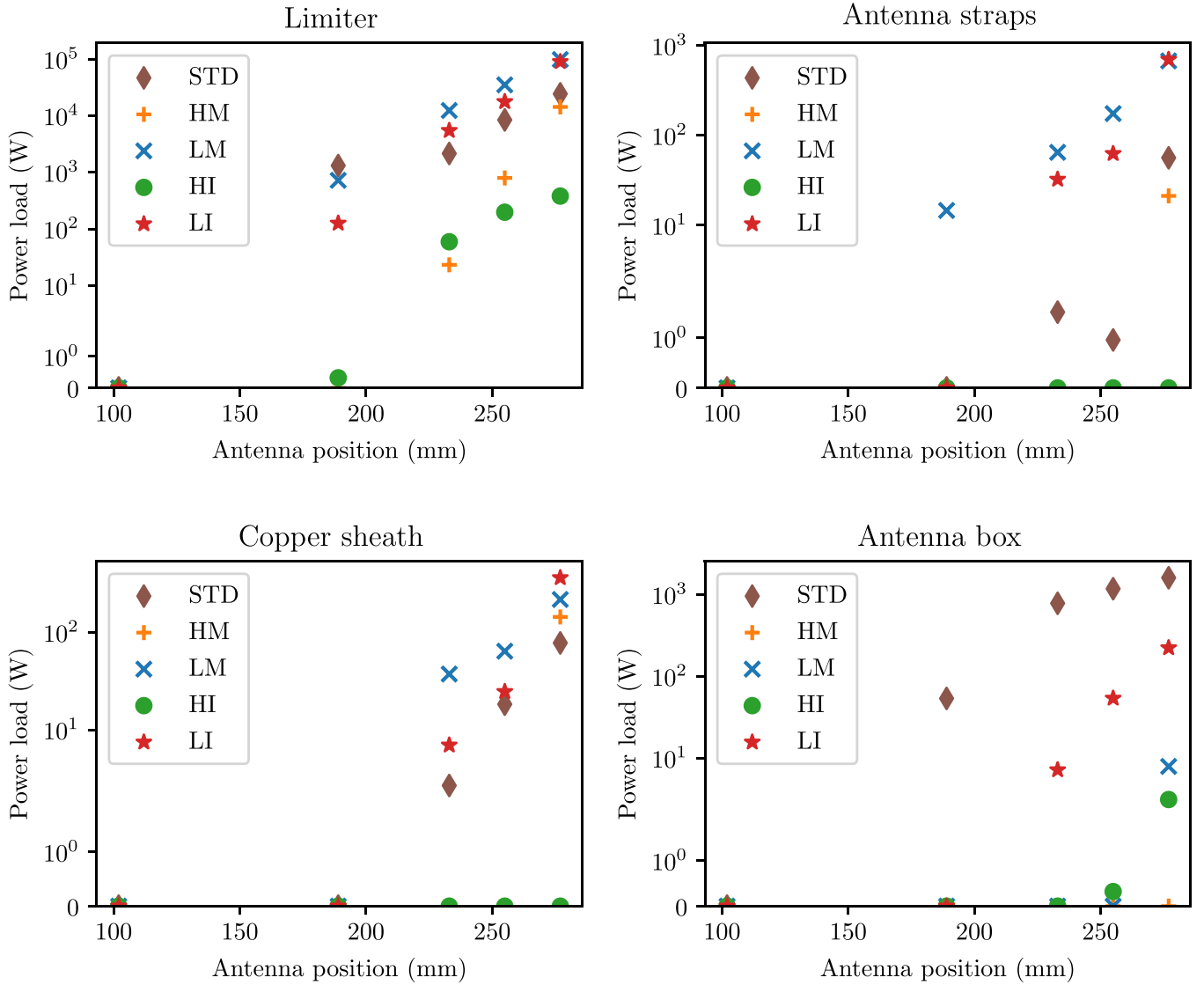


Figure 8. NBI ion power load to the ICRH antenna components in all of the studied magnetic configurations. The power load is shown as a function of the distance of the antenna to the park position.

focused on the upper left- and right-most parts of the straps, with LI also exhibiting loads in the lower left-most part.

The copper sheath loads exhibit a slightly different ordering for the highest total loads. The LI configuration still has the highest loads at up to 360 W, but the LM loads are now clearly lower at 210 W. The HI configuration does not have any loads to the sheath regardless of insertion depth. Interestingly, the HM configuration has somewhat higher loads than standard for the copper sheath. This is because according to figure 6, the copper sheath loads in all configurations are concentrated on the inner side of the antenna limiter, namely in the upper left corner. In the HM configuration this area is also subject to high power losses to the limiter tiles due to the magnetic field shape.

The antenna box loads exhibit very different behavior to the other components: only the standard configuration has significant loads of up to 1.6 kW. The LI configuration also has a total load of up to 200 W. According to figure 6, the antenna

box loads in the standard and LI configurations are spread along the right-most side of the antenna box.

4.3. Limiter power flux estimates

To further assess the safety of concurrent NBI-ICRH operation, the power flux to the ICRH antenna for each wall model triangle was also calculated. The accuracy of this calculation was limited by the number of markers hitting the antenna components, which was more than 100 000 markers for the antenna limiter, up to 3000 for the antenna straps and box, and less than 500 for the copper sheath in all simulations. This practically means that from these simulations accurate power flux can only be calculated for the antenna limiter. In addition, triangles with only a single hit were excluded from the power flux calculation to avoid single hits to small wall triangles from skewing the results.

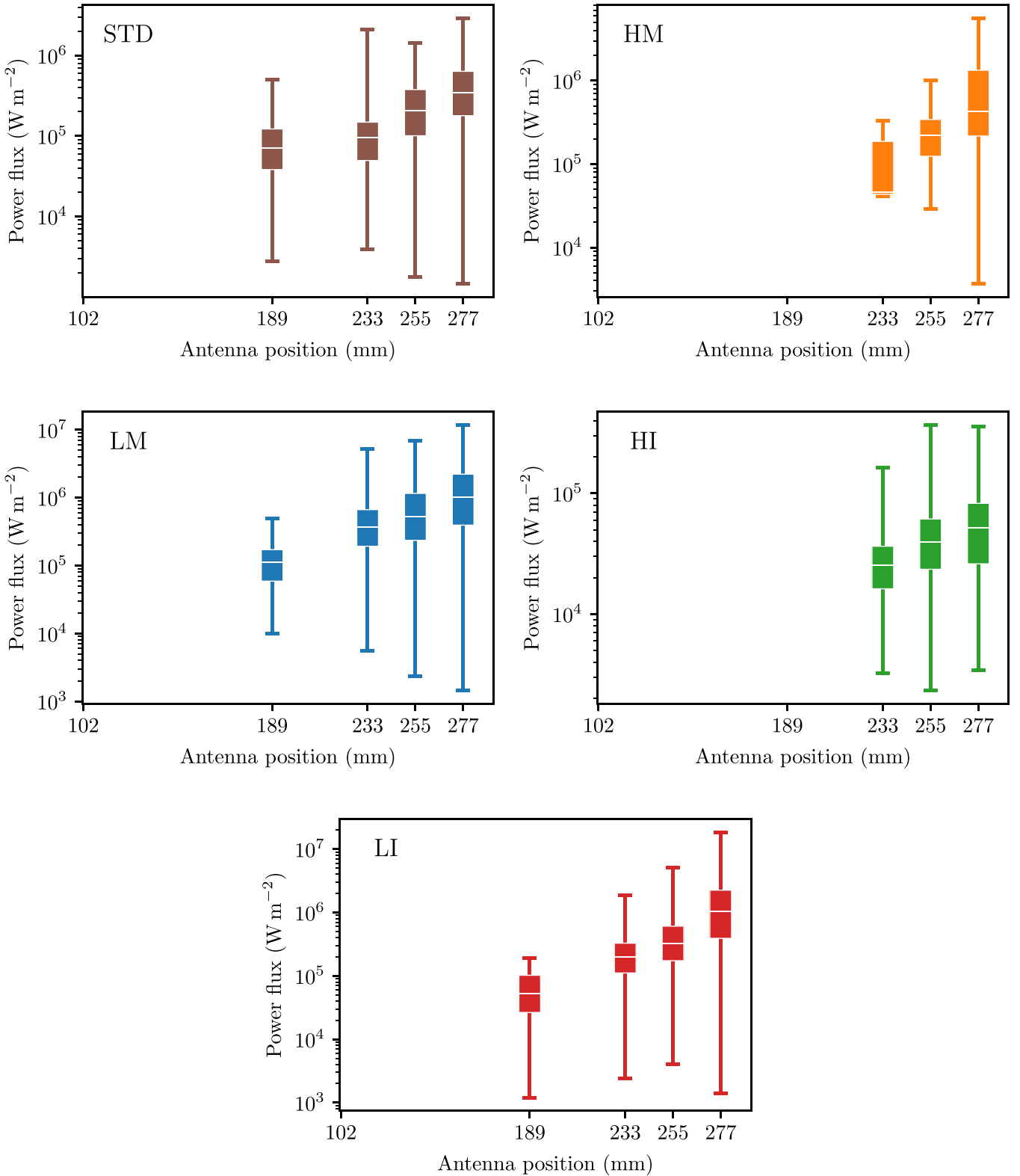


Figure 9. NBI ion power flux to the ICRH antenna limiter for the different magnetic configurations. The power fluxes are shown as a function of the distance of the antenna to the park position. The figure shows the mean (white line), box with lower to upper quartiles, and the total data range (whiskers).

The power flux estimates for the limiter are shown in figure 9. The limiter tiles do not get any power loads in the liner antenna position in any of the configurations. Even at half insertion depth the power fluxes are very low or, in the

case of the HM and HI configurations, non-existent. Closer to the working position significant power fluxes begin to appear—at the working position, the power flux can reach up to 17.5 MW m^{-2} for some limiter triangles in the LI

configuration. In fact, in all but the HI configuration the maximum power fluxes are above the 2 MW m^{-2} steady-state safety limit, even when considering only the NBI power flux and not the thermal and ICRH ion contributions. The mean power flux stays below the safety limit in all configurations, while the upper 75% quartile of power loads are above the safety limit in the LM and LI configurations. However, as mentioned before these safety limits are very conservative for NBI injection, as the maximum NBI pulse length is only 5 s compared to 30 min for steady-state operation. It is therefore likely that the NBI input power flux to the antenna limiter will not limit NBI pulse lengths at least in the operating conditions studied here.

5. Conclusions and further work

The NBI power load to the W7-X ICRH antenna was found to have an exponential dependence on the antenna insertion depth. Significant wall loads are only seen at an insertion of at least 50% between the liner and working positions of the antenna. The LM and LI configurations consistently had the highest power loads, standard the next highest, and the HM and HI configurations the lowest. This is best explained by the distance of the antenna to the LCFS, which is highest in the HM and HI configurations. The HI configuration also has the added benefit of a very thin magnetic island width, which reduces the possible channels of the fast particles hitting the antenna.

The maximum simulated antenna insertion of 277 mm was based on the **designated** working position in the standard magnetic configuration. The actual antenna working positions are planned to vary based on the shape of the LCFS. An recent internal study at Wendelstein 7-X was done to suggest antenna working positions for each magnetic configuration based on thermal heat loads [27]. The suggested positions are summarized in table 4, where the insertion depth normalized to the 277 mm maximum insertion position studied in this work is also shown. In the STD, HI, and HM configurations the suggested insertion depth of the working position is more than 277 mm and the power loads will exceed the highest values obtained in this study. In the LI and LM configurations the insertion depth lies within the range of this study and, thus, the power loads will be less than the highest loads presented here. To evaluate the value for the power load at these configuration-dependent working positions would require additional simulations or extrapolation. However, the main outcome of this work is the qualitative nature of the power load on the insertion depths, not the precise numerical values. Quantitative simulations could be done on a case-by-case basis to obtain more accurate values for certain discharges.

The local power flux to the ICRH antenna limiter was also calculated. Based on the maximum loads, the NBI power flux can exceed the steady-state limiter safety limit of 2 MW m^{-2} in all but the HI configuration. Nevertheless, due to the limited NBI pulse length the NBI power loads should not pose a safety hazard to the limiter tiles.

Table 4. Suggested ICRH antenna operating positions based on thermal load calculations in each of the magnetic configurations.

	Insertion depth (mm)	Normalized to STD working position
STD	281	1.01
HM	299	1.08
LM	267	0.96
HI	317	1.14
LI	262	0.95

For the next operational phase, OP2.1, only four of the eight possible NBI sources that were simulated in this work will be available. This would mean that the magnitude of the calculated NBI power loads would be approximately halved, assuming that the power loads for each symmetrically positioned NBI source are roughly equal. The figures presented here thus represent an upper limit to the NBI power loads to the antenna.

The sensitivity of the wall loads to profile variation was briefly studied during this work using the same plasma profiles as earlier wall load calculations in W7-X [4, 28]. These profiles have approximately four times higher density and two times lower temperature than the parametric profiles presented here. The power loads with alternate profiles were found to be roughly twice that of the values shown here in the standard configuration. This is most likely due to the beam ionization profile skewing closer to the LCFS with higher density. More detailed simulations are needed to fully assess the effect of density scaling, however.

These simulations only cover a small space of possible operating scenarios, and for more accurate predictions in the future several improvements are suggested. First of all, realistic plasma profile measurements should be used once available, in particular to provide better beam deposition calculations. Preferably this would also include an estimate of the density outside the LCFS, at least in front of the NBI ports. Accurate plasma profiles would also be important for assessing CX reactions, which will be implemented in a future version of ASCOT, and would influence the radial electric field profiles as well.

Because ASCOT only provides the fast-ion flux to the wall, they should be combined with FEM calculations to assess the time evolution of the component surface temperature. Only then can proper time limits for NBI injection during ICRH operation be established. This would also require combining the NBI ion power loads calculated here with both thermal and ICRH-heated fast-ion power loads to account for all contributions to the power load. The combined loads could then be validated by monitoring the temperature of the antenna using existing thermocouple and infrared camera diagnostics [11].

Data availability statement

The data cannot be made publicly available upon publication because they are not available in a format that is sufficiently

accessible or reusable by other researchers. The data that support the findings of this study are available upon reasonable request from the authors.

Acknowledgments

The calculations were performed on Marconi-Fusion, the High Performance Computer at the CINECA headquarters in Bologna (Italy). The computational resources provided by Aalto Science-IT project are also acknowledged. This work was partially funded by the Academy of Finland Project No. 298126. This work has been carried out within the framework of the EUROfusion Consortium and has received funding from the Euratom research and training programme 2014–2018 and 2019–2022 under Grant Agreement No. 633053. The views and opinions expressed herein do not necessarily reflect those of the European Commission.

ORCID iDs

J Kontula  <https://orcid.org/0000-0002-0620-6208>
 S Äkäslompolo  <https://orcid.org/0000-0002-9554-5147>
 S Lazerson  <https://orcid.org/0000-0001-8002-0121>
 D Hartmann  <https://orcid.org/0000-0002-3511-6500>
 J Ongena  <https://orcid.org/0000-0001-7456-4739>

References

- [1] Grieger G, Beidler C, Harmeyer E, Lotz W, Kißlinger J, Merkel P, Nührenberg J, Rau F, Strumberger E and Wobig H 1992 Modular stellarator reactors and plans for Wendelstein 7-X *Fusion Technol.* **21** 1767–78
- [2] Wolf R C *et al* 2019 Performance of Wendelstein 7-X stellarator plasmas during the first divertor operation phase *Phys. Plasmas* **26** 082504
- [3] Drevlak M, Geiger J, Helander P and Turkin Y 2014 Fast particle confinement with optimized coil currents in the W7-X stellarator *Nucl. Fusion* **54** 073002
- [4] Äkäslompolo S, Drevlak M, Turkin Y, Bozhnikov S, Jesche T, Kontula J, Kurki-Suonio T and Wolf R C (the W7-X Team) 2018 Modelling of NBI ion wall loads in the W7-X stellarator *Nucl. Fusion* **58** 082010
- [5] Äkäslompolo S *et al* 2019 Armoring of the Wendelstein 7-X divertor-observation immersion-tubes based on NBI fast-ion simulations *Fusion Eng. Des.* **146** 862–5
- [6] Ongena J *et al* 2014 Study and design of the ion cyclotron resonance heating system for the stellarator Wendelstein 7-X *Phys. Plasmas* **21** 061514
- [7] Bosch H-S *et al* 2013 Technical challenges in the construction of the steady-state stellarator Wendelstein 7-X *Nucl. Fusion* **53** 126001
- [8] Faustin J M, Cooper W A, Graves J P, Pfefferlé D and Geiger J 2016 ICRH induced particle losses in Wendelstein 7-X *Plasma Phys. Control. Fusion* **58** 074004
- [9] Machielsen M, Graves J P and Cooper W A 2021 ICRF modelling in 2D and 3D magnetic configurations using a hot plasma model *Plasma Phys. Control. Fusion* **63** 094002
- [10] Castaño Bardawil D *et al* 2021 Design improvements, assembly and testing of the ICRH antenna for W7-X *Fusion Eng. Des.* **166** 112205
- [11] Schweer B *et al* 2017 Development of an ICRH antenna system at W7-X for plasma heating and wall conditioning *Fusion Eng. Des.* **123** 303–8
- [12] Lazerson S A *et al* (the W7-X Team) 2021 Modeling and measurement of energetic particle slowing down in Wendelstein 7-X *Nucl. Fusion* **61** 096005
- [13] Rust N, Heinemann B, Mendelevitch B, Peacock A and Smirnov M 2011 W7-X neutral-beam-injection: selection of the NBI source positions for experiment start-up *Fusion Eng. Des.* **86** 728–31
- [14] Lazerson S A *et al* (the W7-X Team) 2021 First neutral beam experiments on Wendelstein 7-X *Nucl. Fusion* **61** 096008
- [15] Varje J, Särkimäki K, Kontula J, Ollus P, Kurki-Suonio T, Snicker A, Hirvijoki E and Äkäslompolo S 2019 High-performance orbit-following code ASCOT5 for Monte Carlo simulations in fusion plasmas submitted (arXiv:1908.02482)
- [16] Asunta O, Govenius J, Budny R, Gorelenkova M, Tardini G, Kurki-Suonio T, Salmi A and Sipilä S 2015 Modelling neutral beams in fusion devices: beamlet-based model for fast particle simulations *Comput. Phys. Commun.* **188** 33–46
- [17] Sirén P, Varje J, Äkäslompolo S, Asunta O, Giroud C, Kurki-Suonio T and Weisen H 2017 Versatile fusion source integrator AFSI for fast ion and neutron studies in fusion devices *Nucl. Fusion* **58** 016023
- [18] Sipilä S, Varje J, Johnson T, Bilato R, Galdón-Quiroga J, Snicker A, Kurki-Suonio T, Sanchís L, Silvagni D and González-Martín J (the ASDEX Upgrade Team and the EUROfusion MST1 Team) 2021 ASCOT orbit-following simulations of ion cyclotron heating with synthetic fast ion loss diagnostic: a first application to ASDEX upgrade *Nucl. Fusion* **61** 086026
- [19] Hirvijoki E, Decker J, Brizard A J and Embréus O 2015 Guiding-centre transformation of the radiation–reaction force in a non-uniform magnetic field *J. Plasma Phys.* **81** 475810504
- [20] den Harder N, Rittich D, Orozco G and Hopf C 2019 Analytical beamlet code 3D for neutral beam injectors: principles and applications *Plasma Phys. Control. Fusion* **62** 025023
- [21] Nocentini R, Heinemann B, Riedl R, Rust N and Orozco G 2015 Design of the torus interface for the neutral beam injectors of Wendelstein 7-X *Fusion Eng. Des.* **100** 453–60
- [22] Grahl M, Svensson J, Werner A, Andreeva T, Bozhnikov S, Drevlak M, Geiger J, Krychowiak M and Turkin Y 2018 Web services for 3D MHD equilibrium data at Wendelstein 7-X *IEEE Trans. Plasma Sci.* **46** 1114–9
- [23] Beurskens M *et al* (the W7-X Team) 2021 Ion temperature clamping in Wendelstein 7-X electron cyclotron heated plasmas *Nucl. Fusion* **61** 116072
- [24] Smith H 2022 NEOTRANSP (available at: <https://gitlab.mpg.de/smithh/neotransp>)
- [25] Klinger T *et al* 2019 Overview of first Wendelstein 7-X high-performance operation *Nucl. Fusion* **59** 112004
- [26] Faustin J, Cooper W, Graves J, Pfefferlé D and Geiger J 2016 Fast particle loss channels in Wendelstein 7-X *Nucl. Fusion* **56** 092006
- [27] Stepanov I 2021 Calculated operating positions of the ICRH antenna in OP2 *Internal IPP Report* (unpublished)
- [28] Kontula J, Äkäslompolo S, Turkin Y, Bozhnikov S, Rust N and Kurki-Suonio T (the Wendelstein 7-X team) 2017 Predictive modelling of NBI wall loads in W7-X scenarios exhibiting vanishing bootstrap current 2017, *Proc. 44th EPS Conf. on Plasma Physics (Belfast, Northern Ireland)* p 2.146